The Astrophysical Journal, 733:117 (10pp), 2011 June 1 doi:10.1088/0004-637X/733/2/117

DUST EXTINCTION AND METALLICITIES OF STAR-FORMING Lyα EMITTING GALAXIES AT LOW REDSHIFT*

Steven L. Finkelstein[1], Seth H. Cohen[2], John Moustakas[3], Sangeeta Malhotra[2], James E. Rhoads[2], and Casey Papovich[1]
[1] George P. and Cynthia Woods Mitchell Institute for Fundamental Physics and Astronomy, Department of Physics and Astronomy, Texas A&M University, College Station, TX 77843, USA; stevenf@physics.tamu.edu
[2] School of Earth and Space Exploration, Arizona State University, Tempe, AZ 85287, USA
[3] Center for Astrophysics and Space Sciences, University of California, San Diego, La Jolla, CA 92093, USA
Received 2010 May 19; accepted 2011 March 25; published 2011 May 16

ABSTRACT

We present the results of an optical spectroscopic study of 12 *GALEX*-discovered star-forming Lyα emitting galaxies (LAEs) at $z \sim 0.3$. We measure the emission-line fluxes from these galaxies by fitting their observed spectra to stellar population models in order to correct for underlying stellar absorption. We revisit earlier stellar population model fitting results, finding that excluding now-known active galactic nuclei lowers the typical stellar population age and stellar mass of this sample to ∼300 Myr and $\sim 4 \times 10^9\ \mathcal{M}_\odot$, respectively. We calculate their dust extinction using the Balmer decrement, and find a typical visual attenuation of $A_V \sim 0.3$ mag, similar to that seen in some high-redshift LAEs. Comparing the ratios of Lyα/Hα and the Lyα equivalent widths to the measured dust extinction, we find that the interstellar media (ISMs) in these objects appear to be neither enhancing nor seriously attenuating the Lyα equivalent widths, as would be the case in a quasi-clumpy ISM. Lastly, we perform a detailed analysis of the gas-phase metallicities of these galaxies, and we find that most galaxies in our sample have $Z \lesssim 0.4\ Z_\odot$. We find that at a fixed stellar mass, these low-redshift LAE analogs are offset by ∼0.3–0.6 dex lower metallicity from the general galaxy population at similar redshifts based on the local mass–metallicity relationship. This implies that galaxies with Lyα in emission may be systematically more metal-poor than star-forming galaxies at the same stellar mass and redshift, similar to preliminary results at $z \sim 2$.

Key words: galaxies: evolution – galaxies: ISM

Online-only material: color figures

1. INTRODUCTION

Galaxies selected on the basis of a bright Lyα emission line were originally thought to be indicative of primordial galaxies undergoing their first burst of star formation (Partridge & Peebles 1967), though they have recently been shown to be a complicated group of objects. Studies utilizing the technique of spectral energy distribution (SED) fitting have shown that typical narrowband-selected Lyα emitting galaxies (LAEs) appear to be predominantly young and low mass, with ages < 100 Myr and masses $\lesssim$ a few $\times\ 10^9\ \mathcal{M}_\odot$ (e.g., Gawiser et al. 2006; Finkelstein et al. 2007; Pirzkal et al. 2007; Lai et al. 2007; Nilsson et al. 2007). However, in many cases these galaxies also appear to contain some dust; thus they are likely not primordial in nature (e.g., Pirzkal et al. 2007; Lai et al. 2008; Finkelstein et al. 2008, 2009d; Pentericci et al. 2009). In addition, a small fraction of LAEs appear to be more evolved with ages of ∼0.5 Gyr and masses of $\sim 10^{10}\ \mathcal{M}_\odot$, suggesting that there may be multiple populations of LAEs, or perhaps a tail in the distribution of LAE properties toward more evolved objects (e.g., Finkelstein et al. 2009d; Lai et al. 2008; Pentericci et al. 2009). These more evolved LAEs provide a link to the characteristically more evolved Lyman break galaxies (LBGs; e.g., Kornei et al. 2010).

While the stellar masses of galaxies can be reasonably constrained from SED fitting, the remaining properties suffer from degeneracies, and can be poorly constrained in the absence of rest-frame optical detections, especially at high redshift. Specifically, the derived ages, dust extinction, and metallicities are only weakly constrained, as they all redden the observed SED of a given galaxy. While photometry spanning the 4000 Å break can improve the fidelity of age estimates, the extinction can typically only be roughly constrained, and the metallicity not constrained at all. In order to obtain more robust estimates of the physical make-up of LAEs, direct measurements of the extinction and metallicity are necessary. At low redshift, this is typically done using measurements of the flux of nebular emission lines in the rest-frame optical, e.g., using Balmer line ratios to measure the dust extinction, and ratios of metal lines to hydrogen lines to measure the gas-phase metallicities (e.g., Kobulnicky et al. 1999; Pettini & Pagel 2004). Many of these analyses are not currently possible at $z \gtrsim 3$ (though see Maiolino et al. 2008), as these diagnostic lines are shifted into the mid-infrared. From $2 < z < 3$, these measurements are possible using near-infrared spectroscopy on 8–10 m class telescopes (e.g., Erb et al. 2006a; Finkelstein et al. 2011b). However, samples of LAEs at these redshifts are only now being compiled, and the required integration times are long.

Presently, we can use low-redshift analogs to try to understand LAEs at high redshift. Locally, the Lyα properties of star-forming galaxies have been studied in great detail. It was found that Lyα emission can correlate with bright UV (and Hα) emission in some regions of a galaxy, but not in others. It was also shown that Lyα can escape from galaxies even with

* Observations reported here were obtained at the MMT Observatory, a joint facility of the University of Arizona and the Smithsonian Institution. These observations were also based in part on observations made with the NASA *Galaxy Evolution Explorer*. *GALEX* is operated for NASA by the California Institute of Technology under NASA contract NAS5-98034.

a significant dust content, especially if outflows are present in the interstellar medium (ISM; e.g., Kunth et al. 1998; Hayes et al. 2007; Atek et al. 2008; Östlin et al. 2009). These results indicate that the mechanisms which regulate Lyα escape are complicated, which is an important detail to consider when interpreting the results of high-redshift LAEs (e.g., Finkelstein et al. 2011a).

A little further out, Deharveng et al. (2008) published the discovery of ∼100 LAEs at $z \sim 0.3$ using the space-based *Galaxy Evolution Explorer* (*GALEX*) telescope. A study of their luminosity function found that LAEs at low redshift are more rare and less luminous in Lyα than at $z > 3$ (Deharveng et al. 2008; Cowie et al. 2010). In a follow-up study, Finkelstein et al. (2009a) studied the stellar populations of a subsample of 30 of these LAEs, finding that they appear older and more massive than typical high-redshift LAEs. A higher fraction of low-redshift LAEs appear to host active galactic nuclei (AGNs), from ∼15% to 40% (Finkelstein et al. 2009b; Scarlata et al. 2009; Cowie et al. 2010). Cowie et al. (2010) compare the metallicities from the ratio of [N II]/Hα emission from $z \sim 0.3$ LAEs to those of $z \sim 0.3$ continuum-selected galaxies, finding that while the distributions overlap, the LAEs extend to lower metallicties. Scarlata et al. (2009) studied the extinction properties of a subsample of 31 of these $z \sim 0.3$ LAEs, finding that their emission-line ratios were consistent with attenuation from a clumpy distribution of dust. Lastly, Atek et al. (2009) used Hα and Hβ observations from a subset of these galaxies to study the Lyα escape fraction, finding clear evidence for a decreased escape fraction with increased extinction, although some galaxies do exhibit a Lyα escape fraction greater than the continuum, which could imply a clumpy ISM geometry (e.g., Neufeld 1991; Finkelstein et al. 2009d).

In this paper we present the spectra of our sample of 12 *GALEX* LAEs in the Extended Groth Strip (EGS) which are dominated by star-formation activity, first analyzed in Finkelstein et al. (2009a) via SED fitting, and later shown to be devoid of AGN activity in Finkelstein et al. (2009b). In Section 2 of this paper, we present the full spectra of every object in our sample, along with their measured line fluxes. In Section 3, we revisit the typical ages and masses of this sample, comparing to what we earlier derived in Finkelstein et al. (2009a) when knowledge of AGN activity was unknown. We discuss the dust properties and insights into the ISM geometries of our sample in Section 4, and in Section 5, we present metallicity measurements with three separate metallicity indicators, as well as examine the mass–metallicity relation, and the implications it has on LAEs near and far. In Section 6 we present our conclusions. Where applicable, we assume $H_0 = 70$ km s^{-1} Mpc^{-1}, $\Omega_m = 0.3$, and $\Omega_\Lambda = 0.7$.

2. DATA

2.1. Observations and Data Reduction

We obtained spectroscopy of 23 of the 27 previously analyzed LAEs from Finkelstein et al. (2009a) in the EGS, using the Hectospec spectrograph with the 6.5 m MMT telescope (all 27 could not be observed in one configuration, thus this choice of 23 allowed the most simultaneous observations). Hectospec is a multi-fiber spectrograph, with 300 1.″5 fibers covering a 1° diameter field of view at the f/5 focus (Fabricant et al. 2005). Our data were taken in queue mode on 2009 March 19, consisting of 120 minutes of low-resolution grating spectroscopy, with spectral coverage from ∼3650 to 9200 Å, and a spectral resolution of ∼5 Å. The seeing throughout the night was consistently between 0.″6 and 0.″8, and thus much smaller than the Hectospec fibers.

There are two primary pipelines for the reduction of Hectospec data, IDL and IRAF[4] based. We chose to use the IRAF-based pipeline, as it has recently been ported for external use as External SPECROAD (or E-SPECROAD).[5] The reduction consists of three tasks: the first, called `specroad`, makes the master bias, flat, and dark frames. The next task, `specroadcal`, traces the fibers across the chips, creates a dispersion function, and creates the fiber throughput correction. `Specroadcal` prompts the user to interactively fit a wavelength solution, using lines of helium, neon, and argon. We obtained rms residuals from 0.1 to 0.15 Å using 55 lines spanning the entire wavelength range. `Specroadcal` then applies a dispersion correction to the flat frame. The last task, `specroadobj`, reduces all of the object data, using the calibrations made with the previous two tasks, and subtracting the sky which the task computed from an average of the six closest of ∼50 sky fibers placed throughout the Hectospec 1° field (where the flux variation between the fibers was small, typically <10%). The software then splits off the 300 fibers into individual fits files, which we used moving forward. Each of these files contains the wavelength, flux, and flux error array for the specific fiber, where the error spectrum is computed from a variance array that was created from the raw frame and processed through the same reduction steps.

In addition to our primary targets, we also placed fibers on 12 F-type stars from the Sloan Digital Sky Survey (SDSS), which we used to flux calibrate the data. These stars are good calibrators, as they are a compromise between strong hydrogen lines in hotter stars and other atomic lines in cooler stars. For each star, we scaled up a Kurucz (1993) F0V star model to match the fluxes, integrating the model spectrum through the SDSS g', r', and i' filter curves (these three bands were fully encompassed by our wavelength range). We then computed a scale factor for each filter by dividing the model flux from the SDSS catalog flux for the given star. A final scale factor was computed as the mean of the scale factor from the three filters. This scale was then multiplied into the model spectrum. Finally, a calibration array was computed as the scaled up Kurucz model divided by the observed stellar spectrum. This was repeated for each star, with a final calibration array coming from the mean of each of the 12 observed stars. We estimated the accuracy of our flux calibration as the standard deviation of the mean of these 12 observations, which we found to be relatively small, at <8%. The final calibration array was multiplied into our object spectra, which in addition to flux calibration also corrects for the grating transmission function. The full spectra of all 12 star-forming LAEs are shown in Figure 1.

2.2. Spectral Fitting

We measure the emission-line fluxes of the objects in our sample using the method described by Moustakas et al. (2010). Briefly, we fit a non-negative linear combination of Bruzual & Charlot (2003) population synthesis models with instantaneous burst ages ranging from 5 Myr to 10.5 Gyr (the age of the universe at $z \sim 0.25$), assuming the Chabrier (2003) initial mass

[4] IRAF is distributed by the National Optical Astronomy Observatory (NOAO), which is operated by the Association of Universities for Research in Astronomy, Inc. (AURA) under cooperative agreement with the National Science Foundation.

[5] E-SPECROAD is available at http://iparrizar.mnstate.edu/~juan/research/ESPECROAD/index.php.

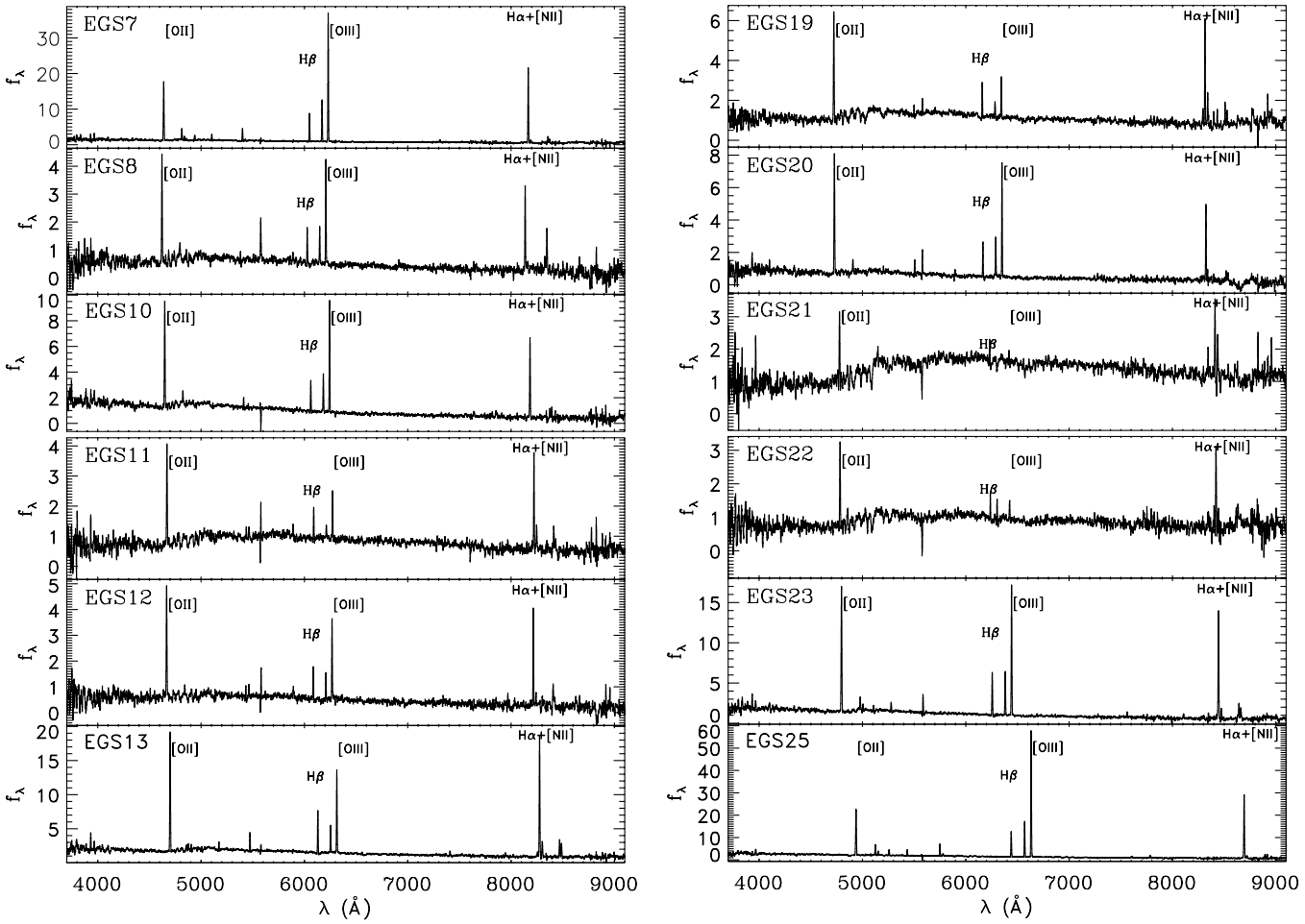

Figure 1. Full Hectospec spectra of the 12 star-forming LAEs in our sample. The vertical axis is in units of 10^{-17} erg s^{-1} cm^{-2} Å^{-1}, and the reader should note that the vertical scale varies from spectrum to spectrum. The typical observed line width is ∼6 Å. In some cases, the 5577 Å atmospheric line is poorly subtracted and should be ignored.

function from 0.1 to 100 $M_\odot$. Motivated by the fact that the gas-phase metallicities of these objects are sub-solar (see Section 5), we assume a fixed stellar metallicity of $Z = 0.004$ ($0.2\,Z_\odot$); however, we have verified that using solar-metallicity templates has a negligible effect on the derived line strengths. After subtracting the best-fitting stellar continuum from the data, we are left with a pure emission-line spectrum self-consistently corrected for underlying stellar absorption. Finally, we fit all the emission lines simultaneously using Gaussian line profiles. In Figure 2, we illustrate our fitting method for one object in our sample, EGS19. In the top panel we plot the observed spectrum (light gray), the best-fitting continuum model (black), and the residual emission-line spectrum (dark gray). We show the full best-fitting emission-line model spectrum (dark red) in the top panel, and in the lower panel we zoom into the emission lines of interest. The lower, middle panel in particular emphasizes the importance of correcting the Hβ line strength for underlying stellar absorption using this kind of technique (see, e.g., Walcher et al. 2011, for a recent review).

The [N II] emission line was not detected in four of our objects. In these cases, we computed upper limits to their line fluxes by adding in mock emission lines to the spectrum, and repeatedly decreasing their line strength until the signal to noise dropped below 3σ. We found that on average, the 3σ line flux limits were $\approx 1.0 \times 10^{-17}$ erg s^{-1} cm^{-2}. In the analysis below, we use the 3σ upper limits as the line fluxes for these lines. Additionally, the [O III] λ4959 line was not detected in two objects (EGS21 and EGS22). This is understandable as these two objects had the lowest [O III] λ5007 fluxes, though both were detected at $>4\sigma$. We thus set the [O III] λ4959 flux to be 0.336 × the [O III] λ5007 flux (the theoretical line flux ratio from Storey & Zeippen 2000) for these two objects. We note that out of the remaining 10 objects, all but two have their ratio of [O III] flux ratios within 3σ of the theoretical value. The line fluxes for the measured lines which are relevant to our analysis are given in Table 1.

3. THE AGES AND MASSES OF STAR-FORMING LOW-REDSHIFT LAEs

In Finkelstein et al. (2009a), we derived the stellar population properties of the parent sample of 30 LAEs via SED fitting, from which we drew the 23 objects observed with Hectospec, including the 12 confirmed star-formation-dominated galaxies presented here. As this was prior to the spectroscopic observations presented in this paper (and Finkelstein et al. 2009b), no knowledge of AGNs or line emission was accounted for in the fitting process. The model templates used in this procedure account only for stellar emission, thus both AGN continuum emission and nebular line emission can cause incorrect fits. Although in this paper we exclude the known AGNs from our

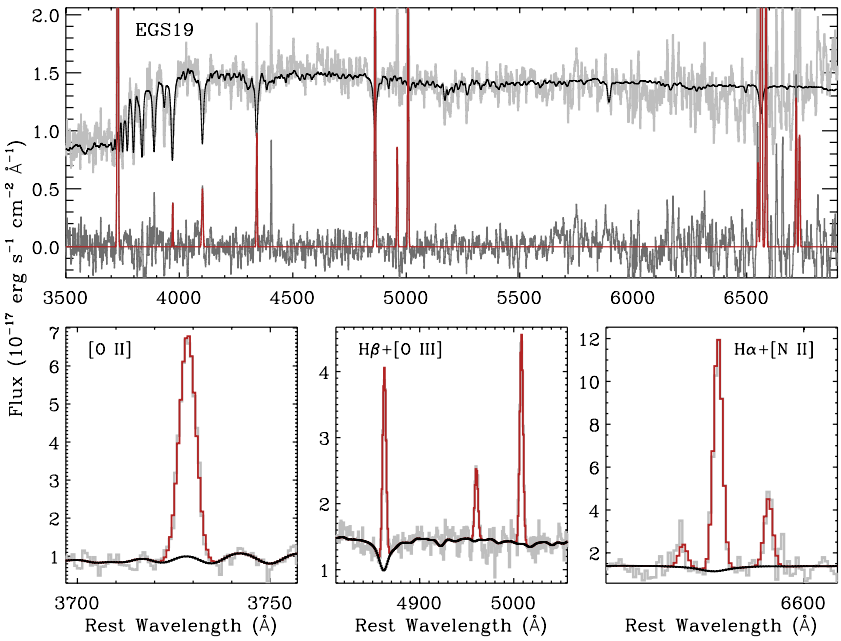

Figure 2. Example of the emission-line fitting method on EGS19. The top panel shows our observed spectrum in gray (smoothed by a 5 pixel boxcar), with the best-fitting spectral model shown as the black curve. The underlying emission-line spectrum, after subtracting the stellar continuum, is shown in red. The bottom three panels show the regions around some of the lines of interest to our study. Of note is the strong stellar Balmer-line absorption. Correcting for this underlying absorption is crucial to an accurate measurement of the Balmer decrement.

(A color version of this figure is available in the online journal.)

Table 1
Object Properties and Measured Line Fluxes

Object	R.A. (J2000)	Decl. (J2000)	Redshift	Lyα λ1216	[O II] λ3727	Hβ λ4861	[O III] λ4959	[O III] λ5007	Hα λ6563	[N II] λ6583
EGS7	214.52132	52.75198	0.2440	27.8	9.58 ± 0.12	5.29 ± 0.08	7.79 ± 0.04	24.03 ± 0.11	19.77 ± 0.20	0.89 ± 0.11
EGS8	214.70103	52.29891	0.2395	15.2	2.25 ± 0.08	0.91 ± 0.06	0.86 ± 0.02	2.52 ± 0.07	2.78 ± 0.10	<0.10
EGS10	215.18036	52.71884	0.2466	28.7	4.80 ± 0.12	1.74 ± 0.06	2.01 ± 0.03	5.93 ± 0.08	6.02 ± 0.16	<0.12
EGS11	214.81132	52.39066	0.2524	14.2	2.05 ± 0.09	0.84 ± 0.06	0.28 ± 0.01	1.06 ± 0.07	2.98 ± 0.10	0.84 ± 0.11
EGS12	215.18599	52.83513	0.2515	25.3	2.59 ± 0.08	1.01 ± 0.05	0.70 ± 0.02	2.12 ± 0.06	3.45 ± 0.12	0.44 ± 0.07
EGS13	214.30073	52.59907	0.2607	20.8	10.52 ± 0.13	4.59 ± 0.08	2.73 ± 0.03	8.43 ± 0.10	17.95 ± 0.21	2.59 ± 0.17
EGS19	214.29112	53.08648	0.2666	22.5	3.13 ± 0.08	1.46 ± 0.06	0.47 ± 0.02	1.40 ± 0.06	5.10 ± 0.15	1.51 ± 0.18
EGS20	214.90226	53.16005	0.2680	17.7	4.65 ± 0.09	1.53 ± 0.07	1.66 ± 0.03	4.80 ± 0.08	4.43 ± 0.11	<0.21
EGS21	214.90685	52.50689	0.2814	18.6	1.39 ± 0.08	0.77 ± 0.07	0.08 ± 0.02	0.25 ± 0.06	2.62 ± 0.16	1.23 ± 0.11
EGS22	214.20791	52.83886	0.2828	17.1	1.47 ± 0.08	0.64 ± 0.08	0.13 ± 0.02	0.40 ± 0.06	2.93 ± 0.18	<0.14
EGS23	214.73294	52.99217	0.2865	29.2	9.75 ± 0.11	4.22 ± 0.09	4.09 ± 0.04	12.43 ± 0.10	15.27 ± 0.20	1.66 ± 0.14
EGS25	214.06925	53.02591	0.3243	25.8	13.89 ± 0.14	8.84 ± 0.10	11.81 ± 0.04	42.91 ± 0.17	31.02 ± 0.24	1.66 ± 0.13

Notes. All line fluxes are in units of 10^{-16} erg s^{-1} cm^{-2}. When [N II] is not detected, we report the 3σ upper limit, as measured from placement of mock lines in the spectra. The Lyα line fluxes are measured from *GALEX* spectra in Deharveng et al. (2008; which have a characteristic uncertainty of 4 × 10^{-16} erg s^{-1} cm^{-2}). The redshift is the weighted mean of all lines detected at $\geqslant 3\sigma$ significance, with a characteristic error $\Delta z \sim 0.00001$.

analysis, it is still prudent to revisit the SED-fitting results as the stellar masses are key to our analysis below.

We have re-performed the SED fitting using the same procedure outlined in Finkelstein et al. (2009a). However, here we use the updated 2007 version of the models of Bruzual & Charlot (2003). In brief, we generate a suite of models, varying the metallicity ($0.02 \leqslant Z \leqslant 2.5\ Z_{\odot}$), star formation history (SFH; exponentially decaying with $10^5 \leqslant \tau_{\rm SFH} \leqslant 10^{9.6}$), stellar population age (10 Myr–$t_{\rm universe}[z]$), dust extinction ($0 \leqslant A_{\rm V} \leqslant 1.6$ mag), and the ISM clumpiness parameter q ($0 \leqslant q \leqslant 10$), where $q = \tau_{\rm Ly\alpha}/\tau_{\rm continuum}$. We fit this suite of models to our observations; *GALEX* far-ultraviolet and near-ultraviolet (FUV and NUV, respectively), Canada–France–Hawaii Telescope Legacy Survey (CHFTLS) u', g', r', i', and z', and the *GALEX* Lyα line flux.

After correcting the observed broadband magnitudes for the emission lines detected in our optical spectra, we compute object colors by dividing the fluxes in all the bands to the u' band. The best-fit model is then found by minimizing the χ^2 between the colors of each object and those of the suite of models. The stellar mass was derived by computing the weighted mean of the observed fluxes to the bandpass-averaged fluxes of the best-fit model. Uncertainties on the best-fit parameters (excepting stellar mass) were computed via a Bayesian likelihood analysis (Kauffmann et al. 2003), where the probability distribution is related to the full χ^2 array via $P \propto e^{-\chi^2/2}$. The χ^2 array is five dimensional—one for each of our free parameters (5 metallicities × 5 SFHs × 124 ages × 21 values of extinction × 10 values of q). Using age as an example, the probability of a given object having a given age is simply the (normalized) total

Table 2
SED-Fitting Results

Object	m_{FUV} (mag)	m_{NUV} (mag)	m_u (mag)	m_g (mag)	m_r (mag)	m_i (mag)	m_z (mag)	Age Best Fit (Myr)	Age 68% Range (Myr)	Mass Best Fit (10^9 $\mathcal{M}_\odot$)	Mass 68% Range (10^9 $\mathcal{M}_\odot$)	A_V Best Fit (mag)	A_V 68% Range (mag)
EGS7	21.63	21.29	21.31	20.88	20.57	20.45	20.48	450	260–800	1.3	1.2–1.5	0.32	0.08–0.57
EGS8	22.03	21.66	21.88	21.18	20.76	20.64	20.63	320	140–400	1.6	1.6–2.1	0.00	0.00–0.40
EGS10	21.59	21.29	21.45	21.02	20.75	20.64	20.60	570	320–900	1.6	1.3–1.7	0.32	0.00–0.49
EGS11	22.16	21.77	21.34	20.58	20.07	19.85	19.73	290	80–360	3.8	3.7–4.9	0.49	0.32–1.05
EGS12	21.64	21.35	21.14	20.42	19.93	19.76	19.64	320	90–2600	4.9	4.8–5.8	0.49	0.16–0.89
EGS13	21.76	21.23	21.24	20.61	20.13	19.93	19.80	810	400–2600	4.2	3.8–7.3	0.57	0.16–0.81
EGS19	21.86	21.29	21.28	20.53	20.03	19.82	19.67	320	180–4200	4.9	4.8–10.8	0.57	0.16–0.89
EGS20	22.02	21.64	21.71	21.21	20.81	20.74	20.66	720	230–1600	2.0	1.7–2.0	0.32	0.08–0.49
EGS21	21.75	21.28	21.11	20.30	19.58	19.29	19.11	9000	2600–8800	34.4	10.5–33.7	0.00	0.00–0.65
EGS22	21.99	21.49	21.32	20.62	20.02	19.82	19.67	260	160–3500	4.8	4.7–4.9	0.65	0.24–0.89
EGS23	21.88	21.37	21.50	21.15	20.82	20.63	20.55	80	27–570	1.1	1.1–2.0	0.97	0.32–1.38
EGS25	22.18	21.10	21.44	21.17	20.95	20.87	20.65	60	18–71	1.2	1.2–2.2	0.97	0.89–1.46

Notes. These magnitudes have had all emission lines detected at $\geqslant 3\sigma$ subtracted. The magnitude errors are 0.2 and 0.02 mag in the *GALEX* and optical bands, respectively (see Finkelstein et al. 2009a).

of P over all other free parameters. As the mass is determined after the selection of the best-fit model, we determine the uncertainty on the masses via 100 Monte Carlo simulations. The emission-line subtracted object magnitudes, best-fit stellar population ages, stellar masses, and dust extinction, as well as the 68% confidence ranges on these parameters are given in Table 2.

In Figure 3, we show histograms of our best-fit stellar population ages and stellar masses, comparing them to the results for the full sample from Finkelstein et al. (2009a). While our earlier study found a number of objects with ages in excess of a Gyr, those primarily appear to be dominated by AGN-hosting LAEs, thus the ages may be unreliable. We find that the updated ages for our star-forming LAE sample are primarily between 100 and 1000 Myr, with a median of ∼300 Myr. We find a similar result for the stellar masses, shown in the bottom plot of Figure 3, in that the many LAEs with derived stellar masses $>10^{10}$ $\mathcal{M}_\odot$ appear to be dominated by AGN hosts, and that the star-forming LAEs in our current sample have masses $\sim 10^9$–10^{10} $\mathcal{M}_\odot$ (with a median of 4×10^9 $\mathcal{M}_\odot$). While these low-redshift LAEs are older and more massive than typical narrowband-selected LAEs, they are similar to those of the more evolved, rarer, LAEs seen at high redshift (e.g., Finkelstein et al. 2009d; Lai et al. 2008; Pentericci et al. 2009). However, we do caution that the derived ages are highly uncertain, as although many objects have best-fit ages on the order of a few hundred Myr, the uncertainties on these derived ages are high—sometimes orders of magnitude. As shown in Table 2, the uncertainties on the stellar masses are much smaller, and we use these best-fit masses with their uncertainties in our metallicity analysis in Section 5.

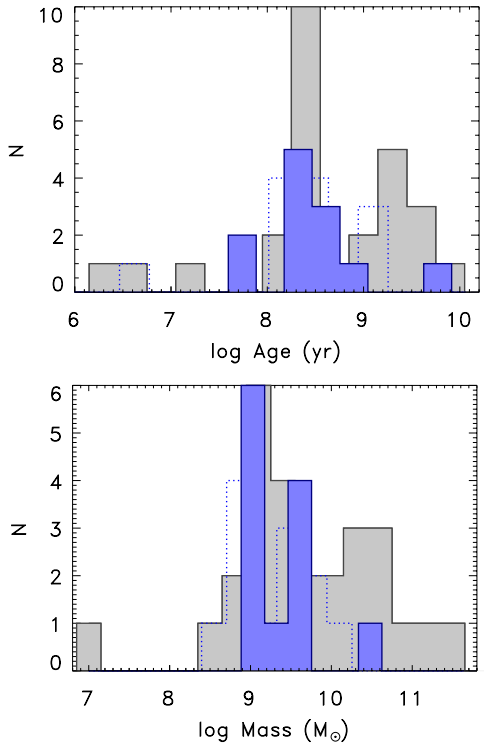

Figure 3. Top: distribution of best-fit stellar populations ages for the 27 LAEs from Finkelstein et al. (2009a) is shown as the gray histogram. The best-fit ages we derive here for the subsample of 12 star-forming LAEs are shown as the blue histogram. While the original sample of 27 LAEs had many objects with best-fit ages >1 Gyr, when we exclude now-known AGNs from Finkelstein et al. (2009b), we find that all but one galaxy appears younger than 1 Gyr. The dotted blue histogram denotes the ages for the same 12 LAEs from Finkelstein et al. (2009a), which broadly agree with our updated results. Bottom: same as the top, for the derived stellar masses. Similar to the ages, a smaller characteristic mass appears likely for these low-redshift LAEs once known AGNs are excluded.

(A color version of this figure is available in the online journal.)

4. DUST EXTINCTION AND THE ISM

Using the Balmer decrement we can measure the level of dust extinction in our galaxies, providing a much more robust estimate than that derived from SED fitting (listed in Table 2). Traditionally, this is done by measuring the ratio of $H\alpha/H\beta$, and then comparing to the theoretical ratio, which we take as $H\alpha/H\beta = 2.86$ (Osterbrock 1989). Any increase in this ratio over the theoretical value is likely due to dust, and, assuming an extinction law, one can compute the color excess. Table 3 tabulates the extinction results assuming the Calzetti et al. (2000) starburst extinction law. The computed color excesses for our objects range from $0 \lesssim E(B-V)_{\rm gas} \lesssim 0.4$, with 10/12 objects having $E(B-V)_{\rm gas}$ significantly greater than zero (at 1σ significance; 9/12 at 2σ). We converted the color excess on the nebular emission to an extinction on the stellar continuum assuming that $E(B-V)_{\rm stellar} = 0.44\,E(B-V)_{\rm gas}$, as has been found locally (Calzetti et al. 2000).

Table 3
Measured Dust Extinction and Gas-phase Metallicities

Object	$E(B-V)_{\rm gas}$	$A_{V,\rm stellar}$ (mag)	$Z_{\rm N2}$ ($Z_\odot$)	$Z_{\rm O3N2}$ ($Z_\odot$)	$Z^l_{\rm R23}$ ($Z_\odot$)	$Z^u_{\rm R23}$ ($Z_\odot$)	Z Weighted Mean ($Z_\odot$)
EGS7	0.23 ± 0.02	0.41 ± 0.04	0.30 ± 0.13	0.27 ± 0.09	0.18 ± 0.03	0.68 ± 0.11	0.20 ± 0.03
EGS8	0.06 ± 0.06	0.11 ± 0.11	0.26[a]	0.29[a]	0.20 ± 0.12	0.86 ± 0.36	0.25 ± 0.07
EGS10	0.16 ± 0.04	0.29 ± 0.07	0.18[a]	0.23[a]	0.28 ± 0.11	0.66 ± 0.20	0.22 ± 0.05
EGS11	0.19 ± 0.07	0.33 ± 0.12	0.85 ± 0.38	0.73 ± 0.26	0.23 ± 0.17	1.11 ± 0.46	0.44 ± 0.13
EGS12	0.15 ± 0.05	0.27 ± 0.10	0.54 ± 0.24	0.48 ± 0.17	0.24 ± 0.13	0.90 ± 0.33	0.36 ± 0.10
EGS13	0.27 ± 0.02	0.47 ± 0.04	0.58 ± 0.24	0.53 ± 0.17	0.24 ± 0.05	0.96 ± 0.15	0.28 ± 0.05
EGS19	0.17 ± 0.05	0.30 ± 0.08	0.87 ± 0.38	0.81 ± 0.28	0.17 ± 0.09	1.31 ± 0.34	0.26 ± 0.08
EGS20	0.01 ± 0.04	0.02 ± 0.08	0.31[a]	0.31[a]	0.25 ± 0.11	0.73 ± 0.24	0.28 ± 0.07
EGS21	0.14 ± 0.09	0.26 ± 0.16	1.13 ± 0.53	1.33 ± 0.52	0.14 ± 0.14	1.74 ± 0.66	1.36 ± 0.33
EGS22	0.40 ± 0.11	0.72 ± 0.21	0.31[a]	0.52[a]	0.38 ± 0.59	1.07 ± 0.85	0.38 ± 0.13
EGS23	0.20 ± 0.02	0.36 ± 0.04	0.49 ± 0.21	0.41 ± 0.13	0.22 ± 0.05	0.80 ± 0.14	0.26 ± 0.05
EGS25	0.17 ± 0.01	0.31 ± 0.03	0.33 ± 0.14	0.28 ± 0.09	0.14 ± 0.02	0.73 ± 0.10	0.15 ± 0.02

Note. [a] [N II] was undetected in EGS8, EGS10, EGS20, and EGS22, and the 3σ upper limit was used on the line flux to compute N2 and O3N2. N2 is thus an upper limit and O3N2 is a lower limit. The weighted mean metallicity was computed with just one value for R23 per object, using the value which gave the lowest error on the weighted mean with the N2 and O3N2 metallicities (which ended up being the lower branch in all cases). The exception is EGS21, where although the weighted mean uncertainty was formally smaller with the lower R23 result, the high metallicities with the O3N2 and N2 indices imply that the upper branch is correct.

We then converted to the stellar attenuation in the V band via the adopted attenuation curve. The derived attenuation on the stellar continuum ranges from $A_{\rm V} = 0$ to 0.7, with a mean $A_{\rm V} \sim 0.3$. Comparing the derived attenuations from the Balmer decrement to those from the photometric SED fitting (listed in Table 2), we find excellent agreement, as the difference in attenuation for 9/12 galaxies is smaller than their combined 1σ uncertainties. This implies that in this sample of galaxies the conversion used from gas extinction to stellar extinction is accurate, and thus that the nebular emission lines are more extincted than the stellar continuum. However, the uncertainties on the Balmer-decrement-derived attenuations are much smaller than those from SED fitting, highlighting the advantage of spectroscopy.

Atek et al. (2009) studied the Lyα escape fraction in LAEs from the $z \sim 0.3$ sample of Deharveng et al. (2008), obtaining spectroscopic measurements of objects from the Chandra Deep Field—South (CDFS) and ELAIS-S1 fields. As part of their analysis, they also computed the dust extinction using the ratio of Hα/Hβ. From their Figure 2, they found values of the color excess from $-0.3 < E(B-V) < 0.5$, covering roughly the same range of color excess values as we find in our independent sample. Atek et al. (2009) find that 12/21 of their objects are consistent with $E(B-V) > 0$. Scarlata et al. (2009) also studied $z \sim 0.3$ LAEs, obtaining optical spectroscopy of 31 galaxies drawn from the Deharveng et al. (2008) EGS, NGPDWS, and SIRTFFL samples, with their EGS sample including four objects in our sample of 12 star-forming galaxies. They do not compute the dust extinction, but to facilitate comparison we have computed the color excess based on their tabulated Hα and Hβ fluxes for the 20 objects which have 3σ detections of both emission lines. Their objects have a range of $-0.05 < E(B-V) < 0.74$, with 11/20 objects consistent with $E(B-V) > 0$ at $>1\sigma$. While both Atek et al. (2009) and Scarlata et al. (2009) find a slightly smaller fraction of objects with significant dust attenuation than we do, this difference is likely due to the small number of objects analyzed in all three studies, as well as the large uncertainties on the extinction in general. We note that Atek et al. (2009) used the extinction curve of Cardelli et al. (1989). Had we adopted this curve, we would have found higher values of the color excess, though the derived attenuation would be similar to what is reported in Table 2.

While many high-redshift LAEs typically have derived non-zero extinctions, these are inferred from SED fitting. As discussed in Finkelstein et al. (2009a) and Section 3, the galaxies in our sample are more evolved than typical narrowband-selected LAEs at high redshift. Thus, it is interesting to compare the mean value of $A_{\rm V} \sim 0.3$ mag measured here to high-redshift LAEs. While Gawiser et al. (2006) derived no dust extinction in LAEs at $z \sim 3.1$, others have frequently found evidence for dust in typical narrowband-selected LAEs. Pirzkal et al. (2007) found $A_{\rm V} = 0$–0.6 mag in LAEs at $z \sim 5$, Lai et al. (2007) found $A_{\rm V} = 0.4$–1.7 mag in LAEs at $z \sim 5.7$, and Finkelstein et al. (2009d) found $A_{\rm V} = 0.1$–1.1 mag in LAEs at $z \sim 4.5$. Thus, though it appears that although high-redshift LAEs are on average younger and lower mass, many of them appear to contain a similar range of dust attenuation as these low-redshift LAEs.

4.1. ISM Geometry

The geometry of the ISM can play a strong role in the escape of Lyα photons. Lyα photons are resonantly scattered by H I, and thus in a homogeneous geometry (i.e., a dust screen in front of the sources) where H I gas and dust are evenly mixed, Lyα has a higher change of getting absorbed by dust than continuum photons, and thus has a difficult time escaping. On the other hand, if the ISM is inhomogeneous, with the dust locked together with neutral gas in many clumps residing in a tenuous, ionized medium, the Lyα photons will resonantly scatter at the edge of these clumps and avoid the dust, while the continuum light will pass through and be subject to dust attenuation (Neufeld 1991; Hansen & Oh 2006). This has the net effect of increasing the Lyα escape fraction over that of the continuum, and thus increasing the Lyα equivalent width (EW). This has been used to explain the large number of high-Lyα EW LAEs which have been found (e.g., Kudritzki et al. 2000; Malhotra & Rhoads 2002). In Finkelstein et al. (2008) and Finkelstein et al. (2009d), we included this scenario in our stellar population models. We parameterized the ISM geometry with a free parameter "q," which is defined by

$$f'_{\rm Ly\alpha} = f_{\rm Ly\alpha} \times \exp(-q\tau_c), \quad (1)$$

where τ_c is the optical depth of dust on the continuum light, thus $q = \tau_{Ly\alpha}/\tau_c$. When $q = 10$, this has the effect of a homogeneous ISM, where Lyα is attenuated far more than the continuum as resonant scattering increases the chance of absorption by dust. When $q = 0$, this simulates the Neufeld (1991) scenario, where all of the dust is locked away inside neutral gas clumps. In between values of q reflect intermediate geometries, with any value of $q < 1$ enhancing the Lyα EW. Using this, we found that dust enhancement can explain the SEDs of many $z \sim 4.5$ LAEs, as 10/14 objects had best-fit $q < 1$. We also used the ISM clumpiness parameter q when we fit models in Finkelstein et al. (2009a) and Section 3 to our sample. Our 12 low-redshift LAEs have a best-fit range from $0 \leqslant q \leqslant 1$, with 5/12 objects having q from 0.75 to 1.0 (using the updated model fitting results discussed in Section 3), reflecting an ISM which does not much enhance or attenuate the Lyα EWs.

With these spectroscopic data, we can now perform a more in depth analysis into the ISM geometry by comparing the resonantly scattered Lyα line to a non-resonant line, such as Hα, as a proxy to trace the continuum photons. Under Case B recombination, the intrinsic ratio of Lyα/Hα is ~8.7. Any deviation from this value is presumably due to dust (although preferential scattering of Lyα photons could play a role). In a typical homogeneous ISM, this value will drop quickly if dust is present. If, however, the ISM is in a configuration that results in the enhancement of the Lyα EW, this value will increase.

Our Hα measurements come from a 1.″5 diameter fiber, while the Lyα measurements are from the FUV *GALEX* prism, which has a beam full width at half-maximum (FWHM) of 4.″2 (Morrissey et al. 2007). As many of these galaxies are larger than 1.″5 (see Figure 1 of Finkelstein et al. 2009a), we need to account for aperture differences between the Lyα and Hα measurements. We did this by first measuring photometry of our sample of galaxies in the CFHTLS i' image (which has a seeing of ~0.″7, comparable to our Hectospec observations), using an aperture diameter of the same size as the Hectospec fibers (1.″5). We then smoothed this image such that the FWHM of stars in the image matched the FWHM of the *GALEX* beam, and performed photometry on our sample again, this time using 4.″2 diameter apertures. In both cases, the photometry was done using the Source Extractor software package (Bertin & Arnouts 1996). The aperture correction which we applied to the Hα flux measurement is thus the ratio of the flux in the 4.″2 aperture to that in the 1.″5 aperture. This aperture correction factor ranged from 1 to 4, with a median of 1.3, and 11/12 galaxies having an aperture correction factor of <2.0 (one object had a correction of <1, which we rounded up to 1).

The left panel in Figure 4 plots the aperture-corrected Lyα/Hα ratios for our sample versus their Hα/Hβ ratios (which is proportional to the derived dust extinction from the previous section). Examining first the Lyα/Hα ratios, we find that they span $1 <$ Lyα/Hα < 7, with all 12 objects having line ratios significantly less than 8.7, implying that dust is likely present. However, the exact amount of dust cannot be derived from this ratio alone as the geometry plays a role. We thus also plot tracks of constant ISM clumpiness from $q = 0$ to 10. By examining where our objects fall in this plane, we can gain insight into their ISM geometry.

Investigating this plane, we find that the majority of our objects are consistent with values of $q \sim 1$–3. This implies that the dust that is present lies in a geometry somewhere between that of a uniform screen and that of purely clumps. In the right panel of Figure 4, we plot the *GALEX* derived Lyα EW versus the Hα/Hβ ratios (and thus the dust extinction). We see that the Lyα EW is between 20 and 40 Å for most objects regardless of the level of extinction. This again implies that the ISM is neither overtly enhancing nor depleting the Lyα EW (similar also to the results from SED fitting). Similar results are seen at $z \sim 2$, where Blanc et al. (2010) recently analyzed a sample of ~100 LAEs and found that Lyα and the rest-frame UV continuum experienced similar levels of extinction (i.e., $q = 1$). As mentioned above, Finkelstein et al. (2009d) found that many $z \sim 4.5$ LAEs were consistent with $q \leqslant 1$, thus at much higher redshift the ISMs may be more clumpy, though this was indirectly inferred via SED fitting.

We note that five of our LAEs are consistent with values of $q < 1$, implying that the ISM could be in a geometry which enhances the observed Lyα EW (i.e., $\tau_{Ly\alpha} < \tau_c$). However, in a clumpy ISM geometry, the dust attenuation law does not necessarily follow the classical $e^{-\tau}$ form (as we assumed above). Natta & Panagia (1984) find that the attenuation law varies with the amount of clumps, in the form of $\exp[-N(1 - e^{-\tau_{c,\lambda}})]$. Only in the limit of a large number of clumps and a moderate optical depth does this tend to the classical attenuation law. We cannot necessarily make these assumptions, so we need to examine how this clumpy attenuation curve matches with our results. In Figure 4 we plot three additional attenuation curves, both assuming N = 5 clumps, for $q = 0$, 1, and 3 (i.e., no Lyα attenuation, Lyα attenuated the same as the UV continuum, and Lyα attenuated more than the UV continuum). At small values of dust extinction, these curves are similar to those from the classical $e^{-\tau}$ attenuation curve. However, as the extinction rises, these curves tend toward higher values of Lyα/Hα. At very high values of extinction, these curves double back, such that the Hα/Hβ values start to decrease. Examining how our potential $q < 1$ objects compare to these curves, we find that this clumpy attenuation law can explain the Lyα/Hα ratios of these LAEs with no need to invoke a value of $q < 1$. Thus, although some form of clumping appears likely in the ISMs of these LAEs, both our observed line ratios and our observed Lyα EWs are consistent with a scenario where Lyα is affected by a similar dust optical depth as the continuum light. For dust enhancement of the Lyα EW to be possible when assuming this clumpy dust law, a Lyα/Hα ratio of $\gtrsim$10 is necessary.

Scarlata et al. (2009) recently investigated the ISMs of a different subsample of LAEs from the Deharveng et al. (2008) sample, examining a number of radiative transfer scenarios, including the clumpy ISM scenario of Natta & Panagia (1984) which we discussed above. They found results similar to ours, in that the line ratios of their objects were consistent with a clumpy interstellar media, but that there is no evidence for preferential shielding of Lyα from dust, as they also do not have any objects with Lyα/Hα > 8.7. Atek et al. (2009) also studied the escape of Lyα photons in their sample of $z \sim 0.3$ LAEs, finding that some objects indicate that a clumpy ISM has contributed to an enhanced Lyα escape fraction ($q < 0$), some objects appear to have similar Lyα and UV-continuum escape fractions ($q \sim 1$), and some objects have Lyα escape fractions < the UV continuum ($q > 1$).

Examining the results for all studied *GALEX* LAEs, it appears that although the ISMs in low-redshift analog LAEs span a wide range of extinction and clumpiness values, some level of clumping appears likely (i.e., a uniform dust screen does not appear to be supported by the data). We note that the necessity of an aperture correction based on photometric data adds a level of overall uncertainty, as it assumes the Hα flux is spatially

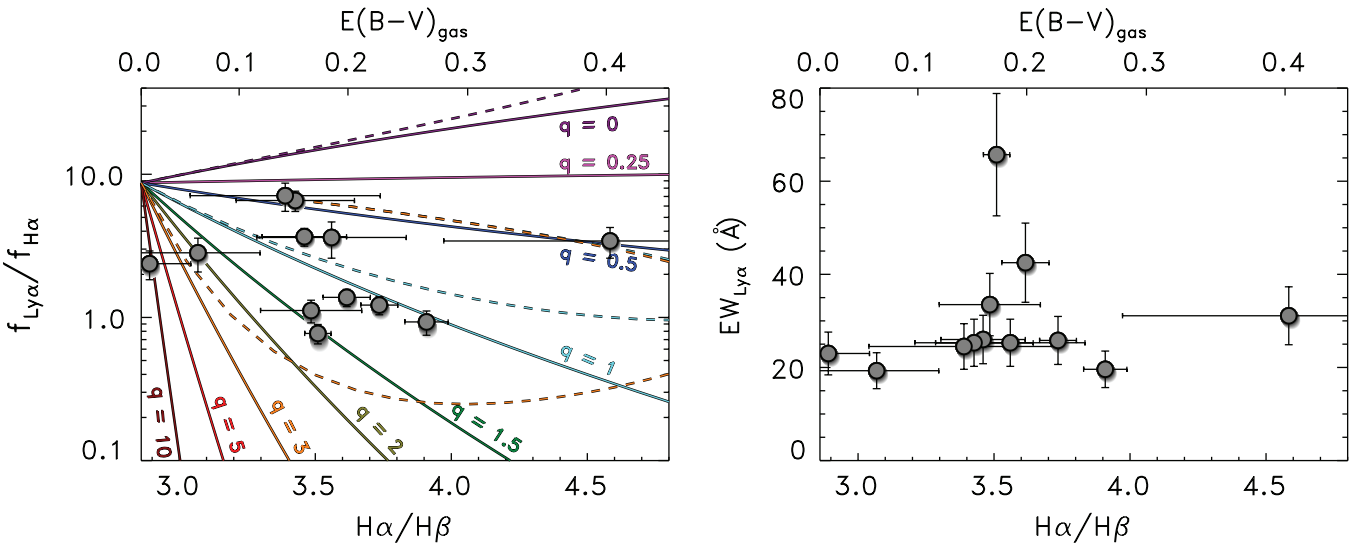

Figure 4. Left: the distribution of Lyα/Hα ratios vs. the observed Hα/Hβ ratios (which are proportional to the dust extinction, as shown on the top horizontal axis) for the 12 star-forming LAEs in our sample. The values of Lyα/Hα have been corrected for aperture differences. The colored lines show model tracks for constant values of q, the ISM clumpiness factor. By studying our objects in this plane, we see that most of the sample lies at $q \sim 1$–3, implying that Lyα encounters a similar level of dust as (and possibly a bit more than) the continuum. At first glance, a few LAEs appear to have an ISM geometry that preferentially favors Lyα escape over continuum photons. However, in a clumpy ISM, the dust law changes from the classical $e^{-\tau}$ form. The dashed lines show the clumpy dust attenuation laws of Natta & Panagia (1984), assuming an average of five clumps per line of sight, for three values of q (0, 1, and 3). We see that the objects above the classical $q = 1$ line can be explained by a clumpy dust attenuation law with $q \geqslant 1$, thus preferential escape of Lyα photons may not be occurring in these galaxies. Right: the Lyα EW vs. the Hα/Hβ ratios, and thus the dust extinction. The EW is roughly invariant to the level of dust, implying that the ISMs of these objects are neither strongly enhancing nor depleting the Lyα EWs, and thus that a uniform dust screen does not apply to these objects.

(A color version of this figure is available in the online journal.)

correlated with the broadband emission. This can be avoided in future studies when both lines are measured in similar apertures.

5. MASS–METALLICITY RELATION

5.1. Gas-phase Metallicity

Using our measured emission lines, we can measure the gas-phase metallicities of the galaxies in our sample with a number of metallicity indices. We can then examine these galaxies on a mass–metallicity relation to see how they compare to other populations. We use ratios of emission lines of oxygen and nitrogen to those of hydrogen to measure the gas-phase metallicities of the galaxies in our sample. Specifically, we use the calibrations of the N2 and O3N2 indices of Pettini & Pagel (2004), where

$$\mathrm{N2} = \log\left(\frac{[\mathrm{N\,II}]}{\mathrm{H}\alpha}\right) \quad (2)$$

and

$$\mathrm{O3N2} = \log\left(\frac{[\mathrm{O\,III}]\lambda 5007/\mathrm{H}\beta}{[\mathrm{N\,II}]/\mathrm{H}\alpha}\right). \quad (3)$$

Additionally, we obtain another measure of the metallicity using the well-known R23 index, where

$$R_{23} = \frac{[\mathrm{O\,II}]\lambda 3727 + [\mathrm{O\,III}]\lambda 4959, 5007}{\mathrm{H}\beta}, \quad (4)$$

using the calibration of Kobulnicky et al. (1999). This index is double valued above $Z \sim 0.3\ Z_{\odot}$; thus, we tabulated the metallicities for both the upper and lower branches. Table 3 presents the measured metallicities of our galaxies from each of these indices, as well as their errors, including systematic uncertainties from the calibrations of 0.05, 0.14, and 0.18 dex for R23, O3N2, and N2 indices, respectively. Prior to this computation, the emission lines were corrected for the inferred dust extinction from Section 4. We note that these indices were calibrated using nearby galaxies, and they may be sensitive to a change in H II region physical conditions such as the ionization parameter or electron temperature. In fact, many high-redshift star-forming galaxies may have an increased ionization parameter as they appear enhanced in [O III]/Hβ from the local star-forming galaxies sequences from the SDSS (e.g., Erb et al. 2006b; Finkelstein et al. 2009c; Hainline et al. 2009). However, as shown in Finkelstein et al. (2009b) the star-forming members of our sample have similar [O III]/Hβ ratios as the SDSS galaxies, thus they likely have similar H II region properties as well.

We also present a weighted mean metallicity from all three measures, where the R23 value which results in smaller uncertainty on the weighted mean was chosen (with the exception of EGS21, where it is obvious that the upper branch of R23 is the appropriate one). In nearly all cases, the three measures of the metallicities are consistent within their uncertainties, thus our results are not dependent on the precise indices used. Investigating Table 3, we find that these low-redshift LAEs typically have metallicities from 0.2 to 0.4 $Z_{\odot}$.

In Figure 5, we plot the 12 star-forming $z \sim 0.3$ LAEs in a mass–metallicity plane. Star-forming galaxies were extensively studied in this plane by Tremonti et al. (2004), who used SDSS spectra of ~53,000 star-forming galaxies to study the mass–metallicity relation at $z \sim 0.1$. In that work, they computed the metallicities by using a combination of all strong emission lines. Because different metallicity indicators suffer inherent systematic uncertainties of 0.2–0.6 dex (Kewley & Dopita 2002; Tremonti et al. 2004; Moustakas et al. 2010), we recomputed metallicities for the SDSS sample using the same techniques as above. In Figure 5 we show the best-fit mass–metallicity relation of Tremonti et al. (2004), which is

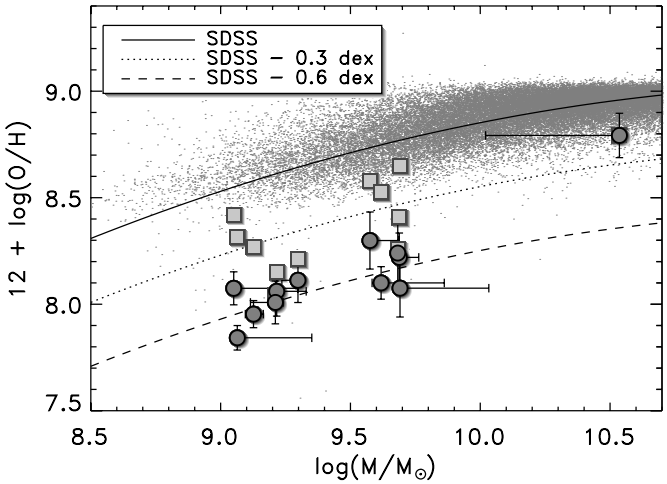

Figure 5. Our sample of 12 star-forming low-redshift LAE analogs plotted in a mass–metallicity plane. Circles denote the metallicities computed using the value of the R23 index which results in the lowest uncertainty on the weighted mean, while squares denote the metallicities assuming the upper R23 branch in the weighted mean. For comparison, we show the sample of ∼53,000 SDSS galaxies from Tremonti et al. (2004), where we recomputed their metallicities using the same methods as our sample. The solid line is the best-fit mass–metallicity relation from Tremonti et al. (2004; shifted down by 0.1 dex to match the sequence shown using our metallicity derivation). The dashed (dotted) line is the SDSS relation shifted downward by ∼0.6 (0.3) dex, highlighting that these LAE analogs are significantly shifted downward in metallicity (regardless of the R23 branch) for a given mass when compared to the SDSS sample. This implies that galaxies exhibiting Lyα in emission may be systematically more metal-poor than other galaxies at the same stellar mass and redshift.

shifted downward by 0.1 dex to match our recomputed SDSS metallicities.

At any given mass, all but the most massive of our $z \sim 0.3$ LAEs lie significantly below the $z \sim 0.1$ mass–metallicity relation. We find that shifting the SDSS mass–metallicity relation downward by ∼0.6 dex best matches our sample of LAEs. This offset is larger than plausible errors in the stellar masses. As there is some ambiguity as to which R23 branch is applicable for these galaxies, we also show where our 12 LAEs would lie if we assumed the upper branch of the R23 index for every LAE when computing the weighted mean metallicity, finding that they still exhibit a 0.3 dex downward shift from the SDSS mass–metallicity relation. These results illustrate that at low-redshift, galaxies exhibiting Lyα in emission have significantly lower metallicities than comparable mass galaxies with no such pre-selection. Cowie et al. (2010) found similar results, as they noted that *GALEX*-selected LAEs had lower metallicities than star-forming galaxies selected via the near-UV continuum. However, their brighter LAEs had metallicities similar to their continuum-selected sample, while all but one of our more massive LAEs are still more metal-poor than the SDSS sample. The differences may be due to the use of solely the N2 index in Cowie et al. (2010), as it typically yields the highest metallicities of the three indicators we use in our sample.

Our comparison sample of SDSS galaxies represents the general star-forming galaxy population at low redshift. At high redshift, LBGs appear to be the dominant galaxy population. Erb et al. (2006b) have studied the mass–metallicity relation of LBGs at $z \sim 2.3$, finding that their objects fit the shape of the local mass–metallicity relation, but shifted downward in metallicity by 0.3 dex (over a metallicity range of 0.4–0.9 $Z_{\odot}$ for galaxies with stellar masses of 10^9–10^{11} $\mathcal{M}_{\odot}$). Current results show that high-redshift LAEs are on average less evolved in age, mass, and dust content than LBGs (e.g,. Gawiser et al. 2006; Finkelstein et al. 2009d; Pentericci et al. 2009), thus it may seem intuitive that they would be lower in metallicity as well (i.e., less evolved in all physical characteristics), possibly shifted even further down for the LBG mass–metallicity relation.

This was recently studied at high redshift by Finkelstein et al. (2011b), where upper limits on the metallicities of two LAEs at $z = 2.3$ and 2.5 were measured to be < 0.17 and 0.28 $Z_{\odot}$, respectively, with the N2 index. The object with the lower metallicity upper limit appears to be significantly below even $z = 2.3$ LBGs on the mass–metallicity relation, similar to our results here at $z \sim 0.3$. Thus, it may be that galaxies exhibiting Lyα in emission have preferentially lower metallicities than the general star-forming galaxy population (i.e., SDSS galaxies at low redshift and LBGs at high redshift). However, the evidence for this at high redshift is not strong, and a confident resolution will not be possible until we can measure the metallicities of large samples of high-redshift LAEs, which will be done with the *James Webb Space Telescope* and the upcoming extremely large telescopes, such as the Giant Magellan Telescope.

6. CONCLUSIONS

We present results from a spectroscopic survey of *GALEX*-discovered LAEs at $z \sim 0.3$. These objects are useful as nearby analogs to high-redshift LAEs, as we are able to directly measure physical quantities which are only inferred at high redshift. In this paper, we present the full optical spectra of 12 star-forming LAEs, including hydrogen, oxygen, and nitrogen line fluxes. We first re-examine their stellar population properties, and find that when excluding the recently identified AGNs in the parent sample, the average ages and masses of the remaining star-forming LAEs are lower at ∼300 Myr and $4 \times 10^9 \mathcal{M}_{\odot}$, respectively. These are older and more massive than a typical high-redshift LAE, but similar to a rare population of evolved high-redshift LAEs.

Correcting our measured emission-line fluxes for stellar absorption, we use the Balmer decrement to investigate the level of dust attenuation in these galaxies. We find that these galaxies all contain some level of dust, with an average extinction of $A_V \sim 0.3$ mag. This is similar to what is typically found at high redshift, and is also consistent with the overall trend of the existence of dust in galaxies which are still able to emit in Lyα. Using the ratio of Lyα/Hα and the measured extinction as a probe of the ISM geometry, we find that in general the ISM geometries for the majority of the sample appear to be somewhere between homogeneous and purely clumpy, implying that a uniform dust screen geometry does not apply to these objects.

Lastly, we use three different metallicity indicators to measure the gas-phase metallicities of the LAEs in our sample. We find that all but one of these galaxies have lower metallicities than continuum-selected star-forming galaxies at the same stellar mass, with typical gas-phase metallicities of ∼0.2–0.4 $Z_{\odot}$. Comparing to recent results at high redshift, it appears that galaxies exhibiting Lyα in emission may be systematically more metal-poor at all redshifts, though more work is needed.

Studying LAEs spectroscopically allows us to learn about their physical properties in more detail and with greater confidence than with stellar population model fitting. Ideally, these low-redshift LAEs would be used as analogs to allow us to decipher the physical characteristics of high-redshift LAEs. As these

objects studied here are more evolved than typical narrowband-selected high-redshift LAEs, we can only put limits on what we expect to find at high redshift. However, with the numerous multi-object near-infrared spectrographs coming online soon, we can expect to make great progress in understanding LAEs by directly measuring their physical properties at $z \sim 2$–3.

We thank the anonymous referee for an extremely useful report which improved the quality of this paper, as well as Giovanni Cresci for useful comments on the manuscript. S.L.F. is supported by the George P. and Cynthia Woods Mitchell Institute for Fundamental Physics and Astronomy in the Department of Physics and Astronomy at Texas A&M University.

REFERENCES

Atek, H., Kunth, D., Hayes, M., Östlin, G., & Mas-Hesse, J. M. 2008, A&A, 488, 491
Atek, H., Kunth, D., Schaerer, D., Hayes, M., Deharveng, J. M., Östlin, G., & Mas-Hesse, J. M. 2009, A&A, 506, L1
Bertin, E., & Arnouts, S. 1996, A&AS, 117, 393
Blanc, G. A., et al. 2010, ApJ, submitted
Bruzual, G., & Charlot, S. 2003, MNRAS, 344, 1000
Calzetti, D., Armus, L., Bohlin, R. C., Kinney, A. L., Koornneef, J., & Storchi-Bergmann, T. 2000, ApJ, 533, 682
Cardelli, J. A., Clayton, G. C., & Mathis, J. S. 1989, ApJ, 345, 245
Chabrier, G. 2003, PASP, 115, 763
Cowie, L. L., Barger, A. J., & Hu, E. M. 2010, ApJ, 711, 928
Deharveng, J.-M., et al. 2008, ApJ, 680, 1072
Erb, D. K., Shapley, A. E., Pettini, M., Steidel, C. C., Reddy, N. A., & Adelberger, K. L. 2006a, ApJ, 644, 813
Erb, D. K., Steidel, C. C., Shapley, A. E., Pettini, M., Reddy, N. A., & Adelberger, K. L. 2006b, ApJ, 646, 107
Fabricant, D., et al. 2005, PASP, 117, 1411
Finkelstein, S. L., Cohen, S. H., Malhotra, S., & Rhoads, J. E. 2009a, ApJ, 700, 276
Finkelstein, S. L., Cohen, S. H., Malhotra, S., Rhoads, J. E., Papovich, C., Zheng, Z. Y., & Wang, J. 2009b, ApJ, 703, L162
Finkelstein, S. L., Papovich, C., Rudnick, G., Egami, E., Le Floc'h, E., Rieke, M. J., Rigby, J. R., & Willmer, C. N. A. 2009c, ApJ, 700, 376
Finkelstein, S. L., Rhoads, J. E., Malhotra, S., & Grogin, N. 2009d, ApJ, 691, 465
Finkelstein, S. L., Rhoads, J. E., Malhotra, S., Grogin, N., & Wang, J. 2008, ApJ, 678, 655
Finkelstein, S. L., Rhoads, J. E., Malhotra, S., Pirzkal, N., & Wang, J. 2007, ApJ, 660, 1023
Finkelstein, S. L., et al. 2011a, ApJ, in press (arXiv:1008.0634)
Finkelstein, S. L., et al. 2011b, ApJ, 729, 140
Gawiser, E., et al. 2006, ApJS, 162, 1
Hainline, K. N., Shapley, A. E., Kornei, K. A., Pettini, M., Buckley-Geer, E., Allam, S. S., & Tucker, D. L. 2009, ApJ, 701, 52
Hansen, M., & Oh, S. P. 2006, MNRAS, 367, 979
Hayes, M., Östlin, G., Atek, H., Kunth, D., Mas-Hesse, J. M., Leitherer, C., Jiménez-Bailón, E., & Adamo, A. 2007, MNRAS, 382, 1465
Kauffmann, G., et al. 2003, MNRAS, 341, 33
Kewley, L. J., & Dopita, M. A. 2002, ApJS, 142, 35
Kobulnicky, H. A., Kennicutt, R. C., Jr., & Pizagno, J. L. 1999, ApJ, 514, 544
Kornei, K. A., Shapley, A. E., Erb, D. K., Steidel, C. C., Reddy, N. A., Pettini, M., & Bogosavljević, M. 2010, ApJ, 711, 693
Kudritzki, R., et al. 2000, ApJ, 536, 19
Kunth, D., Mas-Hesse, J. M., Terlevich, E., Terlevich, R., Lequeux, J., & Fall, S. M. 1998, A&A, 334, 11
Kurucz, R. L. 1993, SYNTHE Spectrum Synthesis Programs and Line Data, CD-ROM (Cambridge, MA: Smithsonian Astrophysical Observatory)
Lai, K., Huang, J.-S., Fazio, G., Cowie, L. L., Hu, E. M., & Kakazu, Y. 2007, ApJ, 655, 704
Lai, K., et al. 2008, ApJ, 674, 70
Maiolino, R., et al. 2008, A&A, 488, 463
Malhotra, S., & Rhoads, J. E. 2002, ApJ, 565, L71
Morrissey, P., et al. 2007, ApJS, 173, 682
Moustakas, J., Kennicutt, R. C., Jr., Tremonti, C. A., Dale, D. A., Smith, J., & Calzetti, D. 2010, ApJS, 190, 233
Natta, A., & Panagia, N. 1984, ApJ, 287, 228
Neufeld, D. A. 1991, ApJ, 370, L85
Nilsson, K. K., et al. 2007, A&A, 471, 71
Osterbrock, D. E. 1989, Astrophysics of Gaseous Nebulae and Active Galactic Nuclei (Mill Valley, CA: Univ. Science Books)
Östlin, G., Hayes, M., Kunth, D., Mas-Hesse, J. M., Leitherer, C., Petrosian, A., & Atek, H. 2009, AJ, 138, 923
Partridge, R. B., & Peebles, P. J. E. 1967, ApJ, 147, 868
Pentericci, L., Grazian, A., Fontana, A., Castellano, M., Giallongo, E., Salimbeni, S., & Santini, P. 2009, A&A, 494, 553
Pettini, M., & Pagel, B. E. J. 2004, MNRAS, 348, L59
Pirzkal, N., Malhotra, S., Rhoads, J. E., & Xu, C. 2007, ApJ, 667, 49
Scarlata, C., et al. 2009, ApJ, 704, L98
Storey, P. J., & Zeippen, C. J. 2000, MNRAS, 312, 813
Tremonti, C. A., et al. 2004, ApJ, 613, 898
Walcher, J., Groves, B., Budavári, T., & Dale, D. 2011, Ap&SS, 331, 1